

Preventing Interdiffusion during Synthesis of Ni-Rich Core–Shell Cathode Materials

Divya Rathore, Matthew Garayt, Yulong Liu, Chenxi Geng, Michel Johnson, J. R. Dahn,* and Chongyin Yang*



Cite This: *ACS Energy Lett.* 2022, 7, 2189–2195



Read Online

ACCESS |



Metrics & More

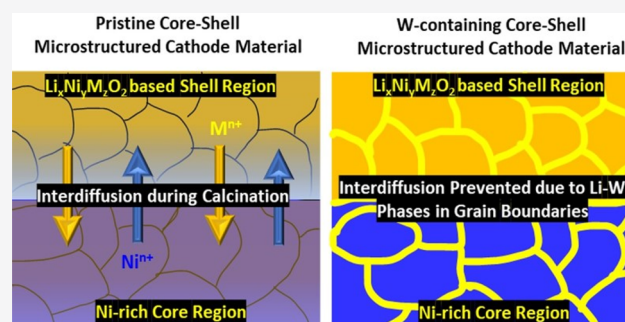


Article Recommendations



Supporting Information

ABSTRACT: Surface reactions between Ni-rich cathode materials and electrolytes limit the achievable specific capacity and lifetime in the high energy density Li-ion batteries based on these cathode materials. A core–shell approach, which contains a less reactive shell-phase on top of a high-capacity core-phase, can be used to reduce these surface reactions. However, interdiffusion of the elements in the core and shell phases can occur during calcination, which limits the choice of elements to be used in the shell phase and the temperature window of synthesis, and often increases the minimum shell thickness. Tungsten oxide (WO_3) coating on the surface of precursors leads to the formation of $\text{Li}_x\text{W}_y\text{O}_z$ secondary phases during the heat treatment with $\text{LiOH}\cdot\text{H}_2\text{O}$. These $\text{Li}_x\text{W}_y\text{O}_z$ phases infuse into the grain boundaries and prevent interdiffusion between the core and shell phases. Tungsten-containing Ni-rich core–shell cathode materials with Mn- or Al-based shells show enhanced electrochemical performance because of reduced surface reactivity due to the core–shell microstructure and additional mechanical strength owing to the presence of $\text{Li}_x\text{W}_y\text{O}_z$ phases in the grain boundaries.



There is a tremendous demand for Li-ion batteries in both the transport sector and power sector to reduce their respective greenhouse emissions in the coming years.¹ The estimated scale of required Li-ion batteries across consumer electronics, stationary storage, and transportation will reach TWh scales by 2030.² Enhancing the lifetimes of high volumetric and gravimetric energy density batteries is critical to make battery electric vehicles (BEVs) more efficient and to enable vehicle to grid (V2G) operation while vehicles are parked, without compromising the cumulative driving range of the vehicle.³ This has led to global research efforts toward optimizing both bulk and surface properties to improve the lifetime of high density layered Ni-rich oxide materials.⁴

One approach to increase the lifetime of Ni-rich cathode materials is to reduce the relative amount of Ni at the surface of the particles. Unwanted reactions such as surface reconstruction from layered to disordered rock-salt, electrolyte reactions with highly reactive surface Ni^{4+} species at a high state of delithiation, gas generation, and safety limitations, etc., can all be directly correlated with high Ni content at the surface.^{5–8} Core–shell or concentration gradient hydroxide precursors have been proposed where some Mg, Co, Mn, or Al is substituted for Ni near the surface of secondary particles while maintaining a Ni-rich core for high energy density.^{9–11} This is a good approach; however, these substituents are prone

to interdiffusion to the core during the heat treatment with $\text{LiOH}\cdot\text{H}_2\text{O}$, making the surface passivation less effective.^{12,13}

It is challenging to prevent interdiffusion with Mg- and Al-based shells even when using a considerable shell thickness.¹⁴ Moreover, an increase in shell thickness compromises the energy density of these Ni-rich cathode materials. Mn-based shells are less prone to interdiffusion but at smaller thicknesses, they still can interdiffuse to the core during the synthesis.¹⁵ Generally, to prevent interdiffusion in such designs, the temperature or heating time needs to be limited, which may compromise the crystallinity of the layered material and therefore its electrochemical performance.¹⁶ Interdiffusion has been identified as a major challenge to overcome for the preservation of core–shell or other special microstructure designs after heat treatment.¹⁷

Coatings of high-valence metal compounds have been explored in Ni-rich materials, including those with W, Ti, Ta, Sb, Nb, etc.^{18–21} Tungsten addition has been reported

Received: April 29, 2022

Accepted: May 31, 2022

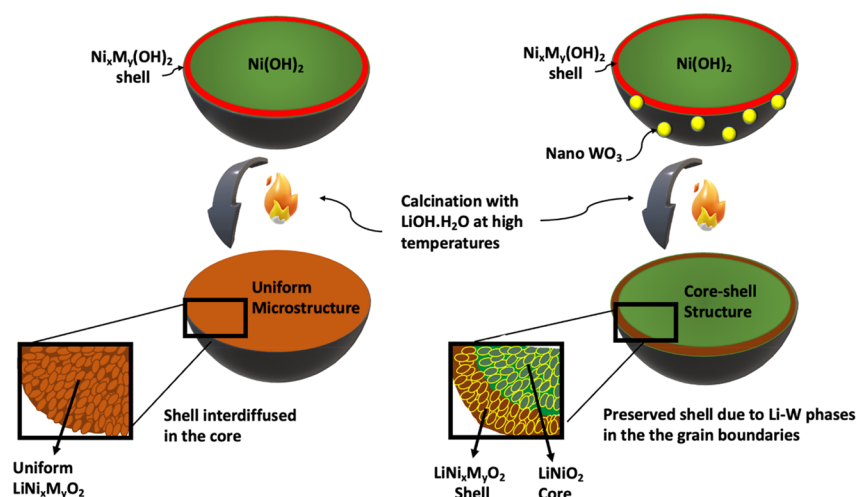


Figure 1. Schematic showing the challenge of interdiffusion in core–shell structured particles during synthesis and the preservation of the initial microstructure in WO_3 coated precursors after calcination due to presence of $\text{Li}_x\text{W}_y\text{O}_z$ phases (shown in yellow) in the grain boundaries. In this work, M can be Mn or Al.

previously to improve the performance and recently published work shows that W does not substitute into the TM layer but rather stays in the grain boundaries in the form of $\text{Li}_x\text{W}_y\text{O}_z$ secondary phases.^{22–26} This behavior is not unique to W. Mo, Nb, and Sb are also observed to be enriched at grain boundaries.^{27,28} The formation of secondary phases in the grain boundaries can potentially act as a barrier to prevent interdiffusion of transition metals during synthesis, therefore, making it possible to synthesize core–shell and other microstructures even with elements like Mg and Al which ordinarily diffuse rapidly. Stable thin shells may also be possible to produce without compromising the optimum synthesis temperature.

This work shows that the addition of 1% W through dry particle coating on hydroxide precursors²⁹ can prevent interdiffusion in thin Mn-rich core–shell microstructures as shown in the schematic in Figure 1. W addition also prevents Al interdiffusion from Al-rich shells even at relatively high synthesis temperatures like 800 °C. Cross-sectional energy dispersive spectroscopy (EDS) line scans show that Mn and Al present in the shell in the precursor are found to be uniformly distributed throughout the bulk in materials without W after synthesis, while they are perfectly preserved in their initial spatial distribution under the same synthesis conditions after the addition of W. These materials containing W, with intact core–shell structure, also outperform all core–shell materials due to the additional benefits of optimal synthesis and the presence of $\text{Li}_x\text{W}_y\text{O}_z$ phases in the grain boundaries. The addition of elements like W, which form secondary phases in the grain boundaries, helps overcome the major challenge of interdiffusion in specially designed cathode structures and enables new avenues of cathode material designs.

The synthesized core–shell materials were first characterized by X-ray diffraction (XRD). The XRD patterns shown in Figure S1a suggest good crystalline material for samples with and without tungsten. The expanded 20°–35° region in Figure S1b shows a broad peak resulting from the amorphous $\text{Li}_x\text{W}_y\text{O}_z$ phases in the samples containing W. The peaks visible in 20°–35° region for CS-NiAl-16/01 and W-NiAl-16/01 samples correspond to Li_5AlO_4 phases as reported previously.¹⁶ Tables S2 and S3 show the Rietveld refinement results for the materials synthesized in this work. The core–

shell materials with Mn-rich shells show some increase in the amount of Ni in the Li layer when W is present while the core–shell materials with Al-rich shells show similar values for materials with and without W for the materials synthesized at 800 °C. The variations in the amount of Ni in the Li layer can be caused by the Li-deficiency of the samples due to formation of $\text{Li}_x\text{W}_y\text{O}_z$ phases and Li loss during synthesis.³⁰

Figure S4 shows Williamson-Hall plots of the materials with and without W to help deconvolute differences between crystallite size and inhomogeneous strain in these materials. The results of Rietveld refinement for the full width half-maximum (fwhm) of the $\text{Cu K}\alpha_1$ peaks were used to plot $\text{fwhm} \times \cos(\theta)$ vs $\sin(\theta)$ where θ is the Bragg angle. The slope of a W–H plot is proportional to the inhomogeneous strain in the materials caused by the lattice constant variation in the sample, and the intercept of a W–H plot gives information about the crystallite grain size.^{31,32} In these studies, there is only a head-to-head comparison between the samples so the full width at half-maximum of the $\text{Cu K}\alpha_1$ peak was used, without deconvoluting the instrumental resolution.

All the W-containing samples show a larger value of the y intercept in the W–H plots in Figure S4 than the corresponding materials without W. This indicates smaller crystallite grain size for materials containing W. Figure S6 shows the smaller size of the primary crystallites for the W-containing samples, which agrees with previous studies.^{25,26} The materials without W, CS-NiMn-17/0.5, CS-NiMn-16/01, CS-NiAl-17/0.5, and CS-NiAl-16/01 show slopes of 0.091, 0.157, 0.097, and 0.126 deg, respectively which indicates an increased inhomogeneous strain in the materials which had a larger thickness shell layer in the precursor.¹⁴ Figure S5 shows that the slopes of W–H plots for core–shell materials are larger for synthesis temperatures where the shell remains. Slope values decrease by increasing synthesis temperatures from 750 to 800 °C for CS-NiMn-17/0.5 and CS-NiMn-16/01. The slope values are similar for Al based core–shell materials at both 750 and 800 °C and an Al based shell is not preserved at either of these synthesis temperatures. Zhang et al. also indicate that presence of shell increases the strain in the crystal structure and can be observed as increased slope in W–H plots.¹⁴ Figure S4 shows that the materials which contain W, W-CS-NiMn-17/0.5, W-CS-NiMn-16/01, W-CS-NiAl-17/0.5,

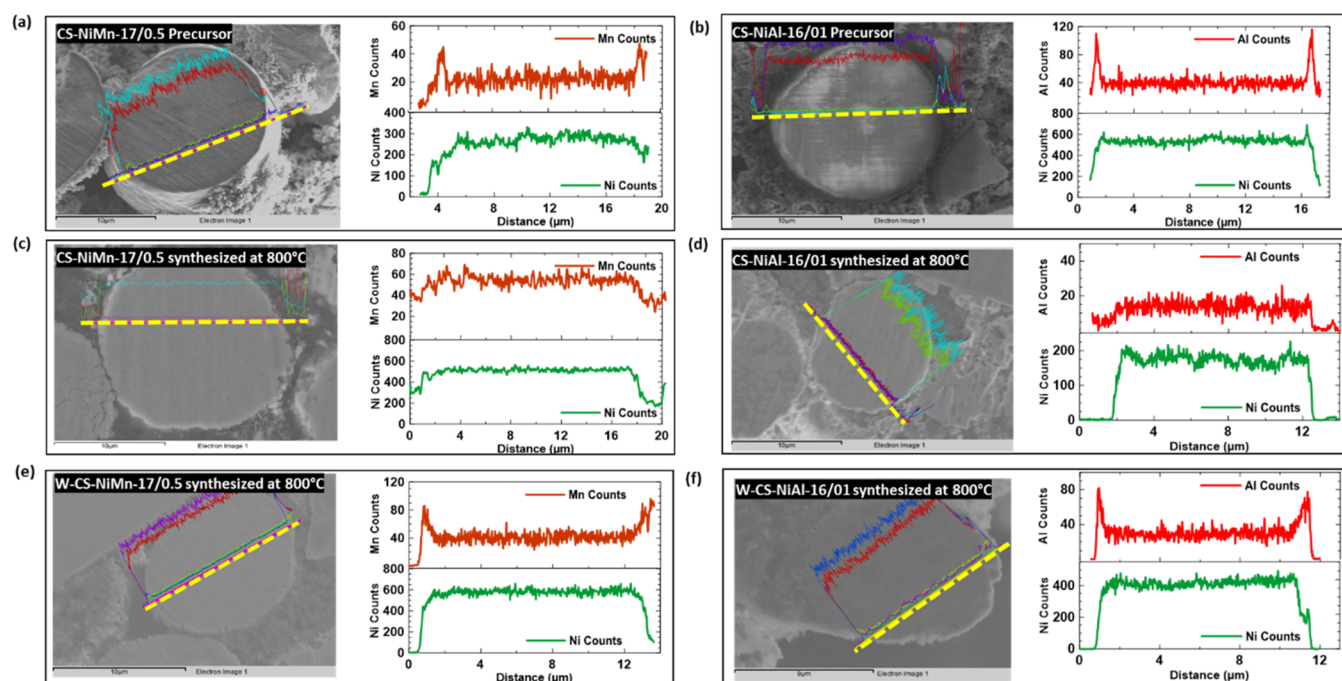


Figure 2. Cross sectional SEM images and EDS line scans of (a) CS-NiMn-17/0.5 hydroxide precursor, (b) CS-NiAl-16/01 hydroxide precursor, (c) CS-NiMn-17/0.5 synthesized at 800 °C, (d) CS-NiAl-16/01 synthesized at 800 °C, (e) 1%W-containing W-CS-NiMn-17/0.5 synthesized at 800 °C, and (f) 1%W-containing W-CS-NiAl-16/01 synthesized at 800 °C

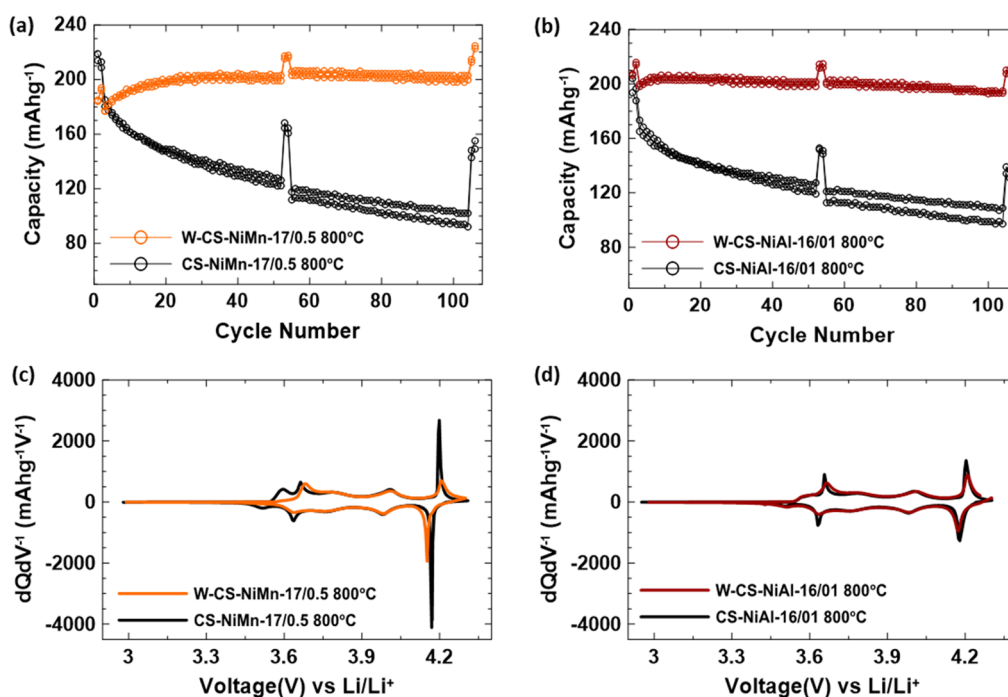


Figure 3. Galvanostatic cycling of (a) CS-NiMn-17/0.5–800C and W-CS-NiMn-17/0.5–800C and (b) CS-NiAl-16/01–800C and W-CS-NiAl-16/01–800C (c, d) Corresponding first cycle differential capacity (dQ/dV) vs voltage curves.

and W-CS-NiAl-16/01, show increased slopes of 0.238, 0.278, 0.240, and 0.244 deg, respectively, compared to the corresponding samples without W. The values of strain in all the W-containing materials are larger than that seen in the materials without tungsten and suggest the preservation of the core–shell structures in all these W-containing materials. The presence of the W-containing phases in grain boundaries prevents the interdiffusion of the core and shell phases, leading

to the presence of two phases with similar, yet different lattice constants, broadening diffraction peaks and creating the increased slope in the W–H plots.

Parts a and b of Figure 2 show EDS line scans over cross section scanning electron microscopy (SEM) images of the hydroxide precursors of CS-NiMn-17/0.5 and CS-NiAl-16/01. These line scans show the Mn and Al signals at the surface corresponding to the $\text{Ni}_{0.8}\text{Mn}_{0.2}(\text{OH})_2$ and $\text{Ni}_{0.8}\text{Al}_{0.2}(\text{OH})_2$

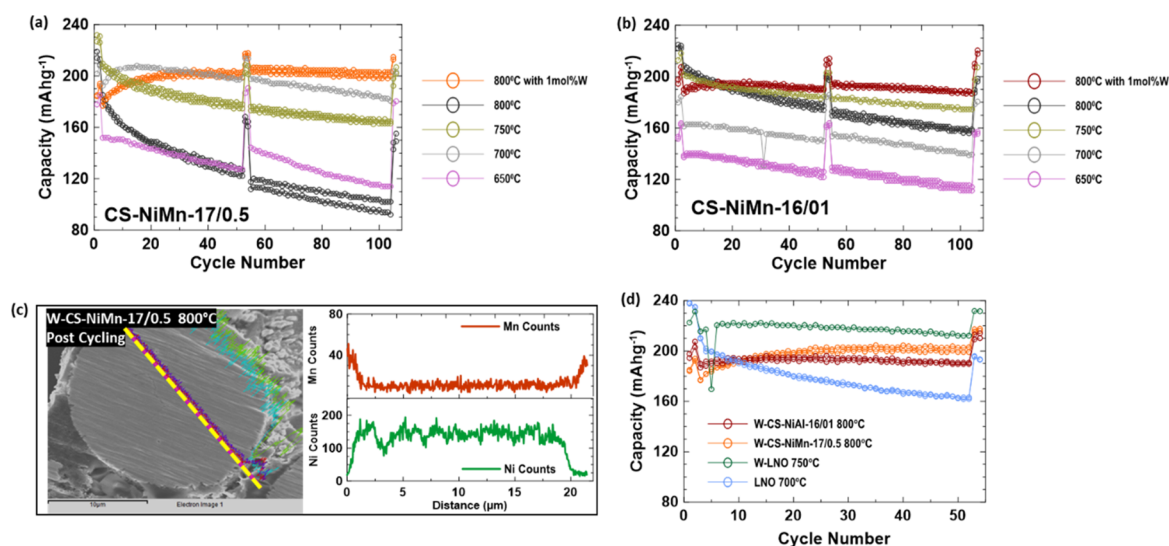


Figure 4. (a) Galvanostatic cycling of CS-NiMn-17/0.5 synthesized at different temperatures compared to W-CS-NiMn-17/0.5. (b) Galvanostatic cycling of CS-NiMn-16/01 synthesized at different temperatures compared to W-CS-NiMn-16/01. (c) Cross-sectional SEM image and EDS line scans of W-CS-NiMn-17/0.5–800C recovered from a half-cell after 100 cycles. (d) Comparison of cycling performance of W-containing core–shell materials with pristine and W-containing LiNiO₂.

shell compositions, respectively. When these materials are lithiated at the synthesis temperature of 800 °C, the shell interdiffuses to the core and no distinguishable Mn or Al signals are observed at the edges of cross section line scans shown in parts c and d of Figure 2. The thin Mn-rich shell used in this study is prone to interdiffusion even at a synthesis temperature of only 750 °C as shown by Liu et al.,¹⁵ while Al-rich shells totally interdiffuse to the core even at 700 °C.¹⁷ By contrast, parts e and f of Figure 2 show that the Mn-rich and Al-rich shells are perfectly maintained for the 1%W-containing materials even at a synthesis temperature of 800 °C. Although the precursor composition is the same, the Li_xW_yO_z phases which form during synthesis infuse into the grain boundaries and inhibit the interdiffusion of the surface metals to the core therefore maintaining the desired core–shell microstructure after lithiation. Figure S7 shows that W-CS-NiMn-16/01 and W-CS-NiAl-17/0.5 also show preserved core–shell structures after lithiation at a synthesis temperature of 800 °C for 20 h.

Charge–discharge cycling shows the dramatically better performance of W-containing materials with preserved Mn-containing and Al-containing shells and Li_xW_yO_z phases in the grain boundaries. The Li_xW_yO_z phases in the grain boundaries provides strength to the polycrystalline particles and prevents microcracking.³³ Figure 3a shows that the specific capacity of CS-NiMn-17/0.5 (no W and core–shell structure eliminated by interdiffusion) after 100 cycles is found to be less than 80% of W-CS-NiMn-17/0.5 (800 °C) (contains W and core–shell structure is intact) after 100 cycles. Figure 3b shows a similar cycling stability for W-CS-NiAl-16/01.

Notably, the reference materials CS-NiMn-17/0.5 and CS-NiAl-16/01 shown in parts a and b of Figure 3 exhibit an unusually poor capacity retention. Figure S8a shows striking secondary particle cracking in cycled CS-NiMn-17/0.5 where significant cracking is occurring. This indicates a poor mechanical strength of these core–shell microstructured materials. Figure S8b shows that the addition of W reinforces the secondary cathode particles structurally.

The capacity increase seen in electrochemical cycling of W-containing materials can be possibly associated with the

evolution of Li_xW_yO_z phases present in grain boundaries during the initial cycling. A good formation protocol strategy or optimization of the amount of W coating might be a possible solution for this capacity creep, which needs to be further explored.

Figure 3c shows suppressed peaks in dQ/dV vs V plots for W-CS-NiMn-17/0.5 (800 °C) compared to CS-NiMn-17/0.5 which is presumably due to the Mn-rich shell phase.¹⁵ Addition of W is seen to suppress the kinetic hindrance region peak below 3.6 V and the H2 → H3 phases transition a remnant peak near 4.2 V during the formation cycle shown in Figure 3c. The intensities of these peaks are also affected by the increased cation mixing for W-containing samples. Figure 3d shows that the addition of W further suppressed the H2 → H3 transition remnant peak for W-CS-NiAl-16/01 compared to CS-NiAl-16/01, which can be associated with the preserved shell structure.

Figure 4a shows that W-CS-NiMn-17/0.5 heated to 800 °C performs better than CS-NiMn-17/0.5 made at the same synthesis temperature and also leads to better specific capacity at the end of 100 cycles due to improved capacity retention in comparison to materials made from the same precursor without W at all the synthesis temperatures tested in this work. Figure 4b shows W-CS-NiMn-16/01 heated at 800 °C has a comparable capacity retention to CS-NiMn-16/01 made at 750 °C. CS-NiMn-16/01 shows quite good capacity retention even without W due to its thicker shell compared to CS-NiMn-17/0.5. However, the thicker shell leads to a compromise in specific capacity. Figure 4c shows a cross-section EDS line scan of W-CS-NiMn-17/0.5 after 100 cycles, which confirms that the thin Mn-rich shell is preserved after cycling. Figure 4d shows that W-CS-NiMn-17/0.5 heated to 800 °C shows the best capacity retention followed by W-CS-NiAl-16/01. These core–shell microstructures outperform W-containing LiNiO₂, prepared from 1% WO₃ coated Ni(OH)₂ heated with LiOH·H₂O in terms of fractional capacity retention.²⁵ All the different W-containing materials shown in Figure 4d show significantly better retention than the simple LiNiO₂ cathode material.

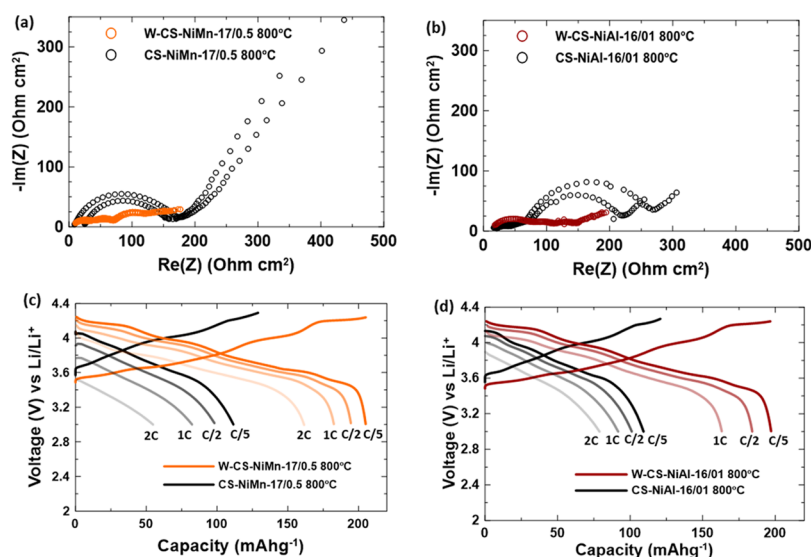


Figure 5. (a) EIS, measured at 10 °C, of half cells at 50%SOC after 100 cycles for CS-NiMn-17/0.5–800C and W-CS-NiMn-17/0.5–800C. (b) EIS, measured at 10 °C, of half cells at 50% SOC after 100 cycles for CS-NiAl-16/01–800C and W-CS-NiAl-16/01–800C. (c) Rate capability test at 30 °C after 100 cycles for CS-NiMn-17/0.5–800C and W-CS-NiMn-17/0.5–800C. (d) Rate capability test at 30 °C after 100 cycles for CS-NiAl-16/01–800C and W-CS-NiAl-16/01–800C.

Electrochemical impedance spectroscopy (EIS) measurements were performed at 3.7 V on the pristine half cells and the cells after 100 cycles. Figure S9 compares EIS of CS-NiMn-16/01 and CS-NiAl-16/01 half cells at 3.7 V with their respective W-coated versions before cycling. W-coated materials for fresh cells show similar impedance spectra as non-W containing materials while parts a and b of Figure 5 show that W-CS-NiMn-17/0.5 and W-CS-NiAl-16/01 after 100 cycles have much lower interfacial and charge transfer resistance than CS-NiMn-17/0.5 and CS-NiAl-16/01, respectively. The W coating is hence observed to be effective in suppressing the impedance increase over cycling by virtue of a preserved shell and the presence of W-based secondary phases in the grain boundaries of the secondary particle.

Figure 5c shows rate capability measurements on half cells of W-CS-NiMn-17/0.5 and CS-NiMn-17/0.5 after 100 cycles. The rate capability of the W-containing sample after 100 cycles is far superior to the sample without W. Figure S9 shows that pristine cells of W-CS-NiMn-16/01 and CS-NiMn-16/01 or W-CS-NiAl-16/01 and CS-NiMn-16/01 show comparable rate capability. The CS-NiMn-17/0.5 material is expected to be reactive with electrolyte since the Mn-rich shell has been eliminated by interdiffusion. This could lead to a greater propensity for forming a surface rock-salt phase over cycling which hinders diffusion. Figure 5d shows similar rate capability studies made on CS-NiAl-16/01 and W-CS-NiAl-16/01 after 100 cycles. In this case, the fractional capacity retained at the various C-rates is similar.

In summary, the presence of $\text{Li}_x\text{W}_y\text{O}_z$ secondary phases in the grain boundaries eliminates the interdiffusion of Mn and Al from the shell to the core in Ni-rich core-shell materials. In addition, the presence of both the intact shell and the $\text{Li}_x\text{W}_y\text{O}_z$ phases in the grain boundaries facilitates better electrochemical performance than materials without W even if the core-shell structure is maintained by using a lower synthesis temperature.

This behavior is probably not unique to W, and it is expected that elements like Mo, Sb, Zr and Nb, which are also found in the grain boundaries, can be used to slow or prevent interdiffusion between core and shell elements.

■ ASSOCIATED CONTENT

Supporting Information

The Supporting Information is available free of charge at <https://pubs.acs.org/doi/10.1021/acseenergylett.2c01009>.

Experimental details, XRD patterns of lithiated materials with W and no W, schematic describing dimensions of core-shell microstructure of precursor, process temperatures recorded during dry particle fusion coating procedure, Williamson-Hall plot comparisons of materials with W and no W at different temperatures, SEM images of lithiated materials, EDS and cross section images of hydroxide precursors and lithiated materials, cross section images post half-cell cycling, EIS and rate capability comparison of fresh cells, and XRD refinement tables of materials discussed in this paper (PDF)

■ AUTHOR INFORMATION

Corresponding Authors

J. R. Dahn – Department of Physics and Atmospheric Science, Dalhousie University, Halifax, Nova Scotia B3H 4R2, Canada; Department of Process Engineering and Applied Science, Dalhousie University, Halifax, Nova Scotia B3H 4R2, Canada; orcid.org/0000-0002-6997-2436; Email: jeff.dahn@dal.ca

Chongyin Yang – Department of Physics and Atmospheric Science, Dalhousie University, Halifax, Nova Scotia B3H 4R2, Canada; orcid.org/0000-0002-7127-3087; Email: c.yang@dal.ca

Authors

Divya Rathore – Department of Physics and Atmospheric Science, Dalhousie University, Halifax, Nova Scotia B3H 4R2, Canada; orcid.org/0000-0003-2909-7726

Matthew Garayt – Department of Physics and Atmospheric Science, Dalhousie University, Halifax, Nova Scotia B3H 4R2, Canada

Yulong Liu – Department of Process Engineering and Applied Science, Dalhousie University, Halifax, Nova Scotia B3H 4R2, Canada

Chenxi Geng – Department of Process Engineering and Applied Science, Dalhousie University, Halifax, Nova Scotia B3H 4R2, Canada

Michel Johnson – Department of Physics and Atmospheric Science, Dalhousie University, Halifax, Nova Scotia B3H 4R2, Canada

Complete contact information is available at:

<https://pubs.acs.org/10.1021/acseenergylett.2c01009>

Notes

The authors declare no competing financial interest.

ACKNOWLEDGMENTS

The authors would like to acknowledge NSERC and Tesla Canada for funding this work under the auspices of the Industrial Research Chair program and the Alliance grant program. Divya Rathore acknowledges the Killam Predoctoral Scholarship Program for financial support. Chenxi Geng acknowledges the China Scholarship Council for financial support. The authors thank Patricia Scallion at the FIB-SEM Facility in the Mechanical Engineering Department at Dalhousie University for help in microscope operation and data collection.

REFERENCES

- (1) Kawamoto, R.; Mochizuki, H.; Moriguchi, Y.; Nakano, T.; Motohashi, M.; Sakai, Y.; Inaba, A. Estimation of CO₂ Emissions of Internal Combustion Engine Vehicle and Battery Electric Vehicle Using LCA. *Sustainability* **2019**, *11* (9), 2690.
- (2) Fichtner, M.; Edström, K.; Ayerbe, E.; Berecibar, M.; Bhowmik, A.; Castelli, I. E.; Clark, S.; Dominko, R.; Erakca, M.; Franco, A. A.; Grimaud, A.; Horstmann, B.; Latz, A.; Lorrmann, H.; Meeus, M.; Narayan, R.; Pammer, F.; Ruhland, J.; Stein, H.; Vegge, T.; Weil, M. Rechargeable Batteries of the Future—The State of the Art from a BATTERY 2030+ Perspective. *Adv. Energy Mater.* **2022**, *12* (17), 2102904.
- (3) Uddin, K.; Dubarry, M.; Glick, M. B. The Viability of Vehicle-to-Grid Operations from a Battery Technology and Policy Perspective. *Energy Policy* **2018**, *113*, 342–347.
- (4) Xie, J.; Lu, Y.-C. A Retrospective on Lithium-Ion Batteries. *Nat. Commun.* **2020**, *11* (1), 2499.
- (5) Jung, R.; Metzger, M.; Maglia, F.; Stinner, C.; Gasteiger, H. A. Oxygen Release and Its Effect on the Cycling Stability of LiNi_xMn_yCo_zO₂ (NMC) Cathode Materials for Li-Ion Batteries. *J. Electrochem. Soc.* **2017**, *164* (7), A1361–A1377.
- (6) Noh, H. J.; Youn, S.; Yoon, C. S.; Sun, Y. K. Comparison of the Structural and Electrochemical Properties of Layered Li[Ni_xCo_yMn_z]-O₂ (x = 1/3, 0.5, 0.6, 0.7, 0.8 and 0.85) Cathode Material for Lithium-Ion Batteries. *J. Power Sources* **2013**, *233*, 121–130.
- (7) Hu, E.; Wang, X.; Yu, X.; Yang, X.-Q. Probing the Complexities of Structural Changes in Layered Oxide Cathode Materials for Li-Ion Batteries during Fast Charge–Discharge Cycling and Heating. *Acc. Chem. Res.* **2018**, *51* (2), 290–298.
- (8) de Biasi, L.; Schiele, A.; Roca-Ayats, M.; Garcia, G.; Brezesinski, T.; Hartmann, P.; Janek, J. Phase Transformation Behavior and Stability of LiNiO₂ Cathode Material for Li-Ion Batteries Obtained from In Situ Gas Analysis and Operando X-Ray Diffraction. *ChemSusChem* **2019**, *12* (10), 2240–2250.
- (9) Myung, S.-T.; Noh, H.-J.; Yoon, S.-J.; Lee, E.-J.; Sun, Y.-K. Progress in High-Capacity Core–Shell Cathode Materials for Rechargeable Lithium Batteries. *J. Phys. Chem. Lett.* **2014**, *5* (4), 671–679.
- (10) Sun, Y.-K.; Myung, S.-T.; Shin, H.-S.; Bae, Y. C.; Yoon, C. S. Novel Core–Shell-Structured Li[(Ni_{0.8}Co_{0.2})_{0.8}(Ni_{0.5}Mn_{0.5})_{0.2}]O₂ via Coprecipitation as Positive Electrode Material for Lithium Secondary Batteries. *J. Phys. Chem. B* **2006**, *110* (13), 6810–6815.
- (11) Hou, P.; Zhang, H.; Zi, Z.; Zhang, L.; Xu, X. Core–Shell and Concentration-Gradient Cathodes Prepared via Co-Precipitation Reaction for Advanced Lithium-Ion Batteries. *J. Mater. Chem. A* **2017**, *5* (9), 4254–4279.
- (12) Liu, Y.; Wu, H.; Li, K.; Li, H.; Ouyang, D.; Arab, P. P.; Phattharasupakun, N.; Rathore, D.; Johnson, M.; Wang, Y.; Yin, S.; Dahn, J. R. Cobalt-Free Core-Shell Structure with High Specific Capacity and Long Cycle Life as an Alternative to Li-[Ni_{0.8}Mn_{0.1}Co_{0.1}]O₂. *J. Electrochem. Soc.* **2020**, *167* (12), 120533.
- (13) Liu, Y.; Ouyang, D.; Rathore, D.; Wu, H.; Li, K.; Wang, Y.; Sha, J.; Yin, S.; Dahn, J. R. An Evaluation of a Systematic Series of Cobalt-Free Ni-Rich Core-Shell Materials as Positive Electrode Materials for Li-Ion Batteries. *J. Electrochem. Soc.* **2021**, *168* (9), 090555.
- (14) Zhang, N.; Zaker, N.; Li, H.; Liu, A.; Inglis, J.; Jing, L.; Li, J.; Li, Y.; Botton, G. A.; Dahn, J. R. Cobalt-Free Nickel-Rich Positive Electrode Materials with a Core–Shell Structure. *Chem. Mater.* **2019**, *31* (24), 10150–10160.
- (15) Liu, Y.; Wu, H.; Wang, Y.; Li, K.; Yin, S.; Dahn, J. R. Impact of Shell Composition, Thickness and Heating Temperature on the Performance of Nickel-Rich Cobalt-Free Core-Shell Materials. *J. Electrochem. Soc.* **2020**, *167* (16), 160556.
- (16) Li, J.; Zhang, N.; Li, H.; Liu, A.; Wang, Y.; Yin, S.; Wu, H.; Dahn, J. R. Impact of the Synthesis Conditions on the Performance of LiNi_xCo_yAl_zO₂ with High Ni and Low Co Content. *J. Electrochem. Soc.* **2018**, *165* (14), A3544–A3557.
- (17) Li, J.; Doig, R.; Camardese, J.; Plucknett, K.; Dahn, J. R. Measurements of Interdiffusion Coefficients of Transition Metals in Layered Li–Ni–Mn–Co Oxide Core–Shell Materials during Sintering. *Chem. Mater.* **2015**, *27* (22), 7765–7773.
- (18) Ryu, H.-H.; Park, G.-T.; Yoon, C. S.; Sun, Y.-K. Suppressing Detrimental Phase Transitions via Tungsten Doping of LiNiO₂ Cathode for Next-Generation Lithium-Ion Batteries. *J. Mater. Chem. A* **2019**, *7* (31), 18580–18588.
- (19) Hwang, D.-Y.; Sim, S.-J.; Jin, B.-S.; Kim, H.-S.; Lee, S.-H. Suppressed Microcracking and F Penetration of Ni-Rich Layered Cathode via the Combined Effects of Titanium Dioxide Doping and Coating. *ACS Appl. Energy Mater.* **2021**, *4* (2), 1743–1751.
- (20) Kim, U. H.; Park, G. T.; Son, B. K.; Nam, G. W.; Liu, J.; Kuo, L. Y.; Kaghazchi, P.; Yoon, C. S.; Sun, Y. K. Heuristic Solution for Achieving Long-Term Cycle Stability for Ni-Rich Layered Cathodes at Full Depth of Discharge. *Nat. Energy* **2020**, *5* (11), 860–869.
- (21) Sun, H. H.; Dolocan, A.; Weeks, J. A.; Heller, A.; Mullins, C. B. Stabilization of a Highly Ni-Rich Layered Oxide Cathode through Flower-Petal Grain Arrays. *ACS Nano* **2020**, *14* (12), 17142–17150.
- (22) Sun, H. H.; Kim, U.-H.; Park, J.-H.; Park, S.-W.; Seo, D.-H.; Heller, A.; Mullins, C. B.; Yoon, C. S.; Sun, Y.-K. Transition Metal-Doped Ni-Rich Layered Cathode Materials for Durable Li-Ion Batteries. *Nat. Commun.* **2021**, *12* (1), 6552.
- (23) Kim, U.-H.; Jun, D.-W.; Park, K.-J.; Zhang, Q.; Kaghazchi, P.; Aurbach, D.; Major, D. T.; Goobes, G.; Dixit, M.; Leifer, N.; Wang, C. M.; Yan, P.; Ahn, D.; Kim, K.-H.; Yoon, C. S.; Sun, Y.-K. Pushing the Limit of Layered Transition Metal Oxide Cathodes for High-Energy Density Rechargeable Li Ion Batteries. *Energy Environ. Sci.* **2018**, *11* (5), 1271–1279.
- (24) Goonetilke, D.; Mazilkin, A.; Weber, D.; Ma, Y.; Fauth, F.; Janek, J.; Brezesinski, T.; Bianchini, M. Single Step Synthesis of W-Modified LiNiO₂ Using an Ammonium Tungstate Flux. *J. Mater. Chem. A* **2022**, *10* (14), 7841–7855.
- (25) Geng, C.; Rathore, D.; Heino, D.; Zhang, N.; Hamam, I.; Zaker, N.; Botton, G. A.; Omessi, R.; Phattharasupakun, N.; Bond, T.; Yang, C.; Dahn, J. R. Mechanism of Action of the Tungsten Dopant in LiNiO₂ Positive Electrode Materials. *Adv. Energy Mater.* **2022**, *12* (6), 2103067.
- (26) Rathore, D.; Geng, C.; Zaker, N.; Hamam, I.; Liu, Y.; Xiao, P.; Botton, G. A.; Dahn, J.; Yang, C. Tungsten Infused Grain Boundaries

Enabling Universal Performance Enhancement of Co-Free Ni-Rich Cathode Materials. *J. Electrochem. Soc.* **2021**, *168* (12), 120514.

(27) Park, G.-T.; Yoon, D. R.; Kim, U.-H.; Namkoong, B.; Lee, J.; Wang, M. M.; Lee, A. C.; Gu, X. W.; Chueh, W. C.; Yoon, C. S.; Sun, Y.-K. Ultrafine-Grained Ni-Rich Layered Cathode for Advanced Li-Ion Batteries. *Energy Environ. Sci.* **2021**, *14* (12), 6616–6626.

(28) Park, N.-Y.; Ryu, H.-H.; Kuo, L.-Y.; Kaghazchi, P.; Yoon, C. S.; Sun, Y.-K. High-Energy Cathodes via Precision Microstructure Tailoring for Next-Generation Electric Vehicles. *ACS Energy Lett.* **2021**, *6* (12), 4195–4202.

(29) Geng, C.; Trussler, S.; Johnson, M. B.; Zaker, N.; Scott, B.; Botton, G.; Dahn, J. R. A Low-Cost Instrument for Dry Particle Fusion Coating of Advanced Electrode Material Particles at the Laboratory Scale. *J. Electrochem. Soc.* **2020**, *167* (11), 110509.

(30) McCalla, E.; Carey, G. H.; Dahn, J. R. Lithium Loss Mechanisms during Synthesis of Layered $\text{Li}_x\text{Ni}_{2-x}\text{O}_2$ for Lithium Ion Batteries. *Solid State Ionics* **2012**, *219*, 11–19.

(31) Williamson, G. K.; Hall, W. H. X-Ray Line Broadening from Filled Aluminium and Wolfram. *Acta Metall* **1953**, *1* (1), 22–31.

(32) Bindu, P.; Thomas, S. Estimation of Lattice Strain in ZnO Nanoparticles: X-Ray Peak Profile Analysis. *J. Theor. Appl. Phys.* **2014**, *8* (4), 123–134.

(33) Hamam, I.; Omessi, R.; Rathore, D.; Geng, C.; Cooke, R.; Plucknett, K.; Bishop, D. P.; Zaker, N.; Botton, G. A.; Yang, C.; Dahn, J. R. Correlating the Mechanical Strength of Positive Electrode Material Particles to Their Capacity Retention. *Cell Reports Phys. Sci.* **2022**, *3* (1), 100714.